Evaluation of $Sn_{0.9}Fe_{0.1}O_{2-\delta}$ as Potential Anode Material for Sodium-Ion Batteries

Anja Lenzer,[a, b] Adele Birrozzi,[a, b] Anna-Lena Wirsching,[a, b] Yueliang Li,[c] Dorin Geiger,[c] Ute Kaiser,[c] Jakob Asenbauer,*[a, b] and Dominic Bresser*[a, b]

The introduction of transition metals such as iron in oxides of alloying elements as, for instance, SnO_2 has been proven to enable higher capacities and superior charge storage performance when used as lithium-ion electrode materials. Herein, we report the evaluation of such electrode materials, precisely (carbon-coated) $Sn_{0.9}Fe_{0.1}O_{2-\delta}(-C)$, for sodium-ion battery applications. The comparison with SnO_2 as reference material reveals the beneficial impact of the presence of iron in the tin oxide lattice, enabling higher specific capacities and a greater reversibility of the de-/sodiation process – just like for lithium-ion battery applications. The overall achievable capacity, however, remains relatively low with about 300 mAh g⁻¹ and up to more than 400 mAh g⁻¹ for $Sn_{0.9}Fe_{0.1}O_{2-\delta}$ and $Sn_{0.9}Fe_{0.1}O_{2-\delta}$-C, respectively, compared to the theoretical specific capacity of more than 1,300 mAh g⁻¹ when assuming a completely reversible alloying and conversion reaction. The subsequently performed *ex situ/operando* XRD and *ex situ* TEM/EDX analysis unveils that this limited capacity results from an incomplete de-/sodiation reaction, thus, providing valuable insights towards an enhanced understanding of alternative reaction mechanisms for sodium-ion anode material candidates.

Introduction

Sodium-ion batteries (SIBs) are at the edge towards commercialization and research on this subject has accordingly triggered a rapidly increasing attention recently.[1,2] This tremendous interest is driven not least by the great need for efficient, versatile, affordable, and sustainable energy storage technologies, and SIBs hold the great promise to provide reasonably high energy and power compared to lithium-ion batteries (LIBs), while making use of much more abundant and cost-efficient materials and components, i.e., sodium instead of lithium as the charge carrier, aluminum instead of copper and hard carbon instead of graphite as current collector and active material for the negative electrode, respectively, and cobalt-free, nickel-poor or even nickel-free and manganese-rich active materials for the positive electrode.[2–7] The replacement of the electrode active materials such as the switch from graphite (LIBs) to hard carbon (SIBs), however, comes amongst others at the expense of achievable specific capacity, i.e., commonly about 300 mAh g⁻¹ (though there is no known theoretical limit) vs. ca. 360 mAh g⁻¹, thus, adding to the generally lower energy density of SIBs.[8–10] In the case of LIBs, conversion,[11–13] alloying,[14–19] and so-called conversion-alloying[20–28] materials provide substantially higher capacities, while alternative anode materials with higher capacities than hard carbon for SIBs remain limited.[29] Among the most studied alternatives are, for instance, antimony[30–32] and phosphorous,[33,34] but antimony is toxic and phosphorus is rather sensitive to the ambient atmosphere owing to its high reactivity.

Following our intensive work on high-capacity conversion-alloying materials (CAMs) for LIBs, we investigated herein the potential use of (carbon-coated) $Sn_{0.9}Fe_{0.1}O_{2-\delta}$ as the most comprehensively investigated Sn-based CAM in LIBs[35,36] concerning its potential applicability as active material for the negative electrode of SIBs. In fact, for LIBs it has been shown that the doping with iron and its reduction to the metallic state leads to an enhanced reversibility of the lithium oxide formation, thus enabling substantially higher capacities.[27,36,37] The favorable effect of the iron doping involves also the formation of smaller Sn nanograins, which further adds to the reversibility of the lithiation reaction. The latter could be further improved by applying a carbon coating, which helps to prevent particle agglomeration upon cycling by buffering the volume variation and providing a physical barrier, while simultaneously corroborating the electron transport within the electrode composite.[23,38] In line with these findings, when studying the de-/sodiation reaction now, the comparison with neat SnO_2 reveals a beneficial impact of the presence of iron in terms of higher specific capacity and enhanced reversibility. Nonetheless, the overall capacity remained relatively low with about 300 mAh g⁻¹ for $Sn_{0.9}Fe_{0.1}O_{2-\delta}$ and 400 mAh g⁻¹ for carbon-coated $Sn_{0.9}Fe_{0.1}O_{2-\delta}$. To understand the origin of these unexpectedly low specific capacities, *operando/ex situ* X-ray

[a] A. Lenzer, Dr. A. Birrozzi, A.-L. Wirsching, Dr. J. Asenbauer, Dr. D. Bresser
Helmholtz Institute Ulm (HIU), 89081 Ulm, Germany
E-mail: jakob.asenbauer@kit.edu
dominic.bresser@kit.edu
Homepage: www.hiu-batteries.de/en/

[b] A. Lenzer, Dr. A. Birrozzi, A.-L. Wirsching, Dr. J. Asenbauer, Dr. D. Bresser
Karlsruhe Institute of Technology (KIT), 76021 Karlsruhe, Germany

[c] Dr. Y. Li, Dr. D. Geiger, Prof. Dr. U. Kaiser
Ulm University, Central Facility for Electron Microscopy, 89081 Ulm, Germany

diffraction and *ex situ* transmission electron microscopy (TEM) coupled with energy-dispersive X-ray spectroscopy (EDX) were conducted, unveiling fundamental insights into the reaction mechanism. Additionally, the use of fluoroethylene carbonate (FEC) as electrolyte additive was studied, highlighting the impact of a suitable solid electrolyte interphase (SEI) on the long-term cycling stability.

Results and Discussion

The comprehensive physicochemical characterization of the three active materials comparatively investigated herein, i.e., SnO_2, $Sn_{0.9}Fe_{0.1}O_{2-\delta}$, and carbon-coated $Sn_{0.9}Fe_{0.1}O_{2-\delta}$ ($Sn_{0.9}Fe_{0.1}O_{2-\delta}$-C) has been reported in an earlier study.[36] To understand the impact of the presence of iron and the carbon coating on the de-/sodiation mechanism, we first performed cyclic voltammetry (CV) in half-cells using sodium metal as the counter electrode. The 1st and 10th cycle are compared in Figure 1(a–c). Generally, the overall shape of the voltammograms appeared very similar for the three different electrode materials. In the first cathodic sweep, all CV plots show a broad peak between 0.4–0.5 V vs. Na^+/Na and a very pronounced peak at < 0.2 V vs. Na^+/Na. The first one has been commonly associated to the decomposition of the electrolyte during the first sodiation, accompanied by the formation of an SEI.[39] This reduction peak is slightly more pronounced for $Sn_{0.9}Fe_{0.1}O_{2-\delta}$-C and even more pronounced for $Sn_{0.9}Fe_{0.1}O_{2-\delta}$ (see also Figure 1d), presumably owing to the simultaneous reduction of iron in this potential range[40] and the high reactivity of iron towards organic carbonate based electrolytes,[41] which is apparently suppressed when the active material has been coated with carbon. The sharp and very intense peak at low potentials (i.e., < 0.2 V) is attributed to the alloying of tin and sodium, along with the insertion of sodium into the non-graphitic (conductive) carbon.[39,42] During the subsequent anodic sweep, two oxidation peaks were observed. The first, very broad one in the range from 0.05 to 0.5 V vs. Na^+/Na has been ascribed to the deinsertion of sodium from the conductive carbon.[39,43] In fact, the direct comparison in Figure 1(d) reveals that there is essentially no difference between the three active materials. The intensity of the second anodic peak at around 0.9–1.0 V vs. Na^+/Na, however, is much more pronounced for $Sn_{0.9}Fe_{0.1}O_{2-\delta}$ and $Sn_{0.9}Fe_{0.1}O_{2-\delta}$-C compared to SnO_2. This might be the result of (i) the reoxidation of iron at such potentials, which is apparently absent in SnO_2, and (ii) a favorable effect of iron on the dealloying and reoxidation of tin. Remarkably, $Sn_{0.9}Fe_{0.1}O_{2-\delta}$-C shows an additional very broad current feature in the elevated potential region at about 1.8 V vs. Na^+/Na where the reconversion is taking place, while this is absent for SnO_2 and $Sn_{0.9}Fe_{0.1}O_{2-\delta}$, indicating that the carbon coating further enhances the reversibility of the sodiation reaction. The 10th cycle shows essentially the same features for all materials. The cathodic peak in the range from 0.05 to 0.5 V, however, largely vanished for SnO_2, while it became more pronounced for $Sn_{0.9}Fe_{0.1}O_{2-\delta}$ and $Sn_{0.9}Fe_{0.1}O_{2-\delta}$-C, along with a shift to
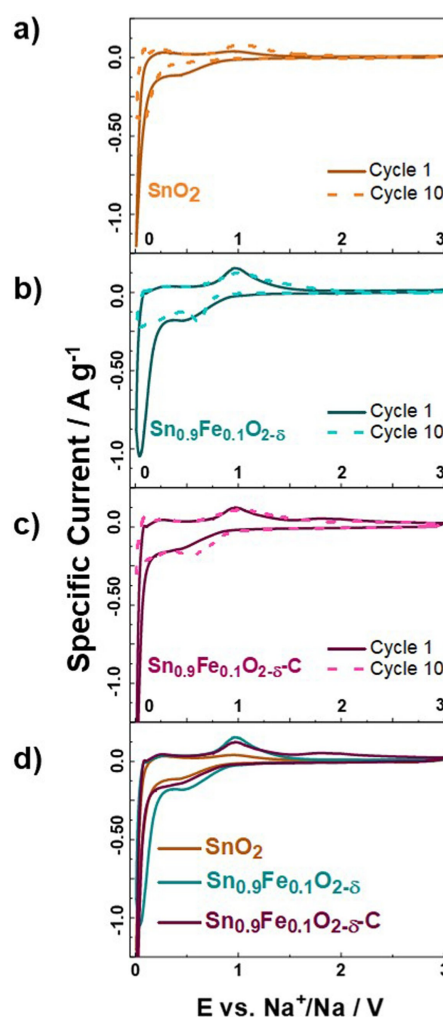
Figure 1. Cycling voltammograms of the 1st (solid line) and 10th (dashed line) cycle of electrodes based on a) SnO_2, b) $Sn_{0.9}Fe_{0.1}O_{2-\delta}$, and c) $Sn_{0.9}Fe_{0.1}O_{2-\delta}$-C as the active material vs. metallic sodium at a sweep rate of 0.1 mV s^{-1} in a voltage range from 0.1 to 3.0 V vs. Na^+/Na. d) Direct comparison of the 1st cycle of all three active materials.

slightly higher potentials, suggesting that the beneficial impact of iron on the sodiation reaction was well maintained.

In a next step, we performed galvanostatic cycling of the three electrodes in half-cells with sodium-metal counter electrodes (Figure 2). The dis-/charge profiles of the 1st and 10th cycle for SnO_2, $Sn_{0.9}Fe_{0.1}O_{2-\delta}$, and $Sn_{0.9}Fe_{0.1}O_{2-\delta}$-C are displayed in Figure 2(a, b, and c), respectively. In all cases, the potential rapidly drops to about 0.8 V vs. Na^+/Na during the first discharge (sodiation), followed by a sloped decrease in the potential range from 0.75 to 0.2 V and a plateau-like feature at about 0.1 V vs. Na^+/Na, which is generally in very good agreement with the CV results (Figure 1). Also, upon charge (desodiation), the sloped plateau at about 1.0 V is in good agreement with the anodic feature in the CV plots, and the trend (in terms of length of this sloped plateau) is the same as the intensity of the anodic peak, i.e., it is longer (meaning higher specific capacity) in the case of $Sn_{0.9}Fe_{0.1}O_{2-\delta}$, and $Sn_{0.9}Fe_{0.1}O_{2-\delta}$-C compared to SnO_2. Moreover, there is subse-
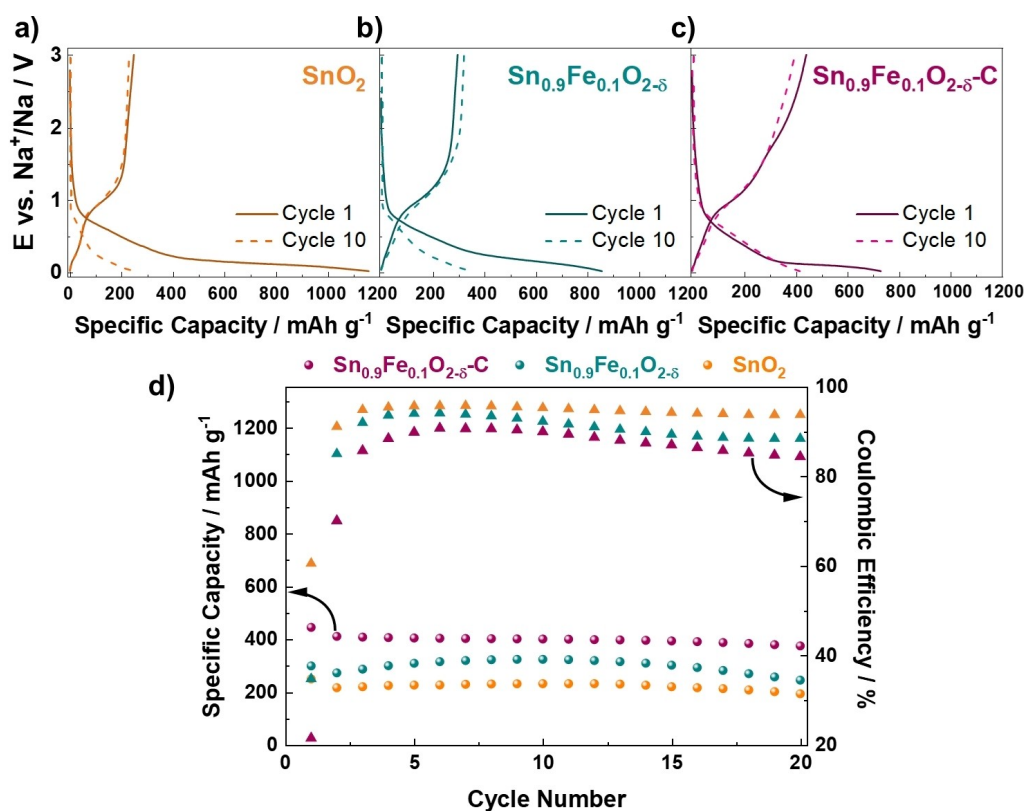
Figure 2. a–c) Dis-/Charge profiles of the 1st (solid line) and 10th (dashed line) galvanostatic cycle at 50 mA g^{-1} and 100 mA g^{-1}, respectively, for a) SnO$_2$, b) Sn$_{0.9}$Fe$_{0.1}$O$_{2-\delta}$, and c) Sn$_{0.9}$Fe$_{0.1}$O$_{2-\delta}$-C vs. metallic sodium. d) Plot of the cycle number vs. specific capacity (desodiation) and Coulombic efficiency for SnO$_2$, Sn$_{0.9}$Fe$_{0.1}$O$_{2-\delta}$ and Sn$_{0.9}$Fe$_{0.1}$O$_{2-\delta}$-C vs. sodium metal (1st cycle: 50 mA g^{-1}; following cycles: 100 mA g^{-1}; cut-off potentials: 0.01 and 3.00 V vs. Na$^+$/Na).

quently a sharp increase in potential for SnO$_2$ and Sn$_{0.9}$Fe$_{0.1}$O$_{2-\delta}$, while there is a further increase in specific capacity for Sn$_{0.9}$Fe$_{0.1}$O$_{2-\delta}$-C beyond this sloped plateau, yielding a total reversible specific capacity of about 444 mAh g^{-1} (compared to ca. 298 mAh g^{-1} for Sn$_{0.9}$Fe$_{0.1}$O$_{2-\delta}$ and 248 mAh g^{-1} for SnO$_2$), which is very well in line with the additional current flow observed in the CV plots. These capacity values are significantly lower than the theoretically expected values of 1,378 mAh g^{-1} (SnO$_2$) and 1,369 mAh g^{-1} (Sn$_{0.9}$Fe$_{0.1}$O$_{2-\delta}$) for a completely reversible conversion and alloying reaction according to the reaction of lithium[23] and taking into account the slightly lower maximum sodium content of the tin alloy of Na$_{3.75}$Sn (note that the formation of Na$_2$O is only an assumption so far)[29,44]:

$$SnO_2 + 4\ Na^+ + 4\ e^- \rightarrow Sn + 2\ Na_2O \qquad (1)$$

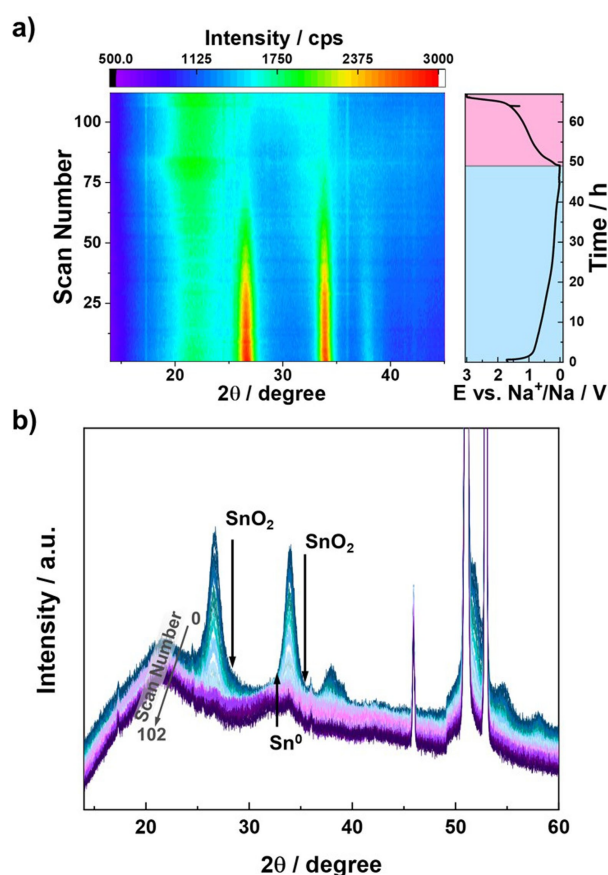$$Sn + 3.75\ Na^+ + 3.75\ e^- \rightarrow Na_{3.75}Sn \qquad (2)$$
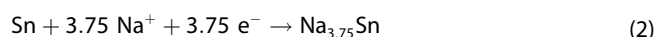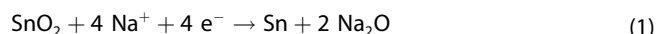
Nonetheless, the results further corroborate the beneficial impact of the iron doping and carbon coating on the reversibility of the sodiation reaction. More precisely, the presence of iron appears beneficial especially for the dealloying reaction at relatively lower potentials, while the carbon coating appears advantageous also for the reconversion reaction occurring at elevated potentials.[23,38,45–47] This enhanced reversibility contributes to a greater first cycle Coulombic efficiency of about 61% in the case of Sn$_{0.9}$Fe$_{0.1}$O$_{2-\delta}$-C and 37% in the case of Sn$_{0.9}$Fe$_{0.1}$O$_{2-\delta}$ compared to only 26% for SnO$_2$. The carbon coating presumably further stabilizes the interface, while the stepwise decrease in initial discharge capacity is presumably also related to the amount of tin in the electrode, which is stepwise decreasing from SnO$_2$ to Sn$_{0.9}$Fe$_{0.1}$O$_{2-\delta}$ by about 10% owing to the replacement of tin by iron in the crystal structure, and further decreasing for Sn$_{0.9}$Fe$_{0.1}$O$_{2-\delta}$-C due to the carbon content of about 13 wt.%.[36]

This stepwise improved reversibility and, thus, increased specific capacity and Coulombic efficiency become even more apparent when plotting the specific capacity and Coulombic efficiency vs. the cycle number (Figure 2d). Sn$_{0.9}$Fe$_{0.1}$O$_{2-\delta}$-C shows the highest specific capacity and Coulombic efficiency across the first 20 cycles, followed by Sn$_{0.9}$Fe$_{0.1}$O$_{2-\delta}$ and SnO$_2$. Moreover, the cycling is most stable for Sn$_{0.9}$Fe$_{0.1}$O$_{2-\delta}$-C, while it starts decreasing for Sn$_{0.9}$Fe$_{0.1}$O$_{2-\delta}$ and SnO$_2$ after 13 cycles and 18 cycles, respectively – along with a significant decline in Coulombic efficiency for the latter two after the first few cycles. Apparently, the carbon coating helps to stabilize the capacity and enhances the reversibility of the sodiation reaction also beyond the first cycle – as also reported earlier for the lithiation reaction.[23] After 20 cycles, Sn$_{0.9}$Fe$_{0.1}$O$_{2-\delta}$-C provides the highest reversible capacity (373 mAh g^{-1}) and Coulombic efficiency (93.8%), followed by Sn$_{0.9}$Fe$_{0.1}$O$_{2-\delta}$ (244 mAh g^{-1} and 88.5%), and SnO$_2$ (192 mAh g^{-1} and 84.4%).

Batteries & Supercaps

Research Article
doi.org/10.1002/batt.202300281

Chemistry Europe
European Chemical
Societies Publishing

To gain more detailed insights into the reaction mechanism and the impact of iron, we conducted *operando* X-ray diffraction (XRD) for $Sn_{0.9}Fe_{0.1}O_{2-\delta}$, accompanied by an *ex situ* XRD analysis of $Sn_{0.9}Fe_{0.1}O_{2-\delta}$-based electrodes after having been fully discharged and fully charged to 0.01 V and 3.0 V, respectively. Figure 3 displays the results of the *operando* XRD investigation with the mapping of the intensity evolution of the reflections and the corresponding dis-/charge profile in Figure 3(a) and the direct comparison of the diffractograms from the pristine to the fully sodiated and fully desodiated state in Figure 3(b). The plots reveal that the reflections attributed to the active material vanish during the first sodiation and small broad reflections appear in the range from 30° to 35°, which are attributed to the formation of metallic tin (see also Figure S1). Any reflections related to the alloy phase, i.e., Na_xSn or sodium oxide are presumably too weak to be detected in the given experimental setup with a beryllium window serving as current collector and "window" for the X-ray beam, or these phases simply remain amorphous and, thus, undetectable by XRD, and/or they are covered by the broad reflection related to metallic tin. Upon desodiation, the sample essentially remains amorphous from the *operando* data, while the broad feature in the range from 30° to 35° remains basically (see also Figure S1).

More insights can be gained from the *ex situ* XRD data obtained for standard electrodes without a beryllium disc on top (Figure 4). When comparing the diffractograms of the pristine electrode with the sodiated (0.01 V) electrode, as depicted in Figure 4(a), it is apparent that the reflections related to the initial tin oxide phase vanished, indicating a complete reduction of the active material. Instead, several new reflections appeared, which can be largely assigned to the formation of metallic tin and a sodium-tin alloy. Given that not all reflections could be assigned to these two phases, it appears reasonable to assume that there are different sodium-tin alloy phases formed rather than only the indexed Na_9Sn_4, which was available from the powder diffraction (PDF) database. Sodium oxide, in fact, has been reported to be amorphous and, hence, not detectable by XRD.[39] Similarly, the diffractogram of the desodiated electrode (Figure 4b) shows several new reflections that could not all be indexed by a comparison with the PDF database. However, there is evidence for the formation of some iron oxide phase along with a tin oxide phase (though less apparent), indicating the reoxidation of the earlier reduced metals. Besides, there are still reflections of metallic tin detectable, suggesting

Figure 3. *Operando* XRD for $Sn_{0.9}Fe_{0.1}O_{2-\delta}$ in sodium half-cell configuration: a) mapping of the measured intensity of the XRD scans as a function of 2θ with the corresponding voltage profile against the time on the right side; b) evolution of the XRD patterns during the first sodiation and de-sodiation.
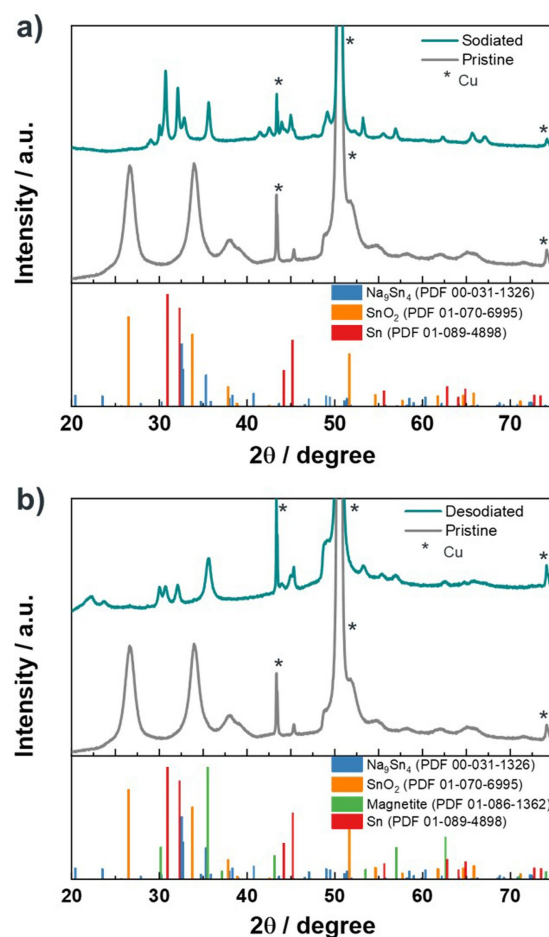
Figure 4. *Ex situ* XRD measurements conducted on a) sodiated (0.01 V) and b) desodiated (3.0 V) $Sn_{0.9}Fe_{0.1}O_{2-\delta}$ electrodes (in turquoise) with the XRD pattern of the pristine electrodes (in grey) for comparison and the corresponding PDF reference data in the bottom. The asterisks mark the reflections corresponding to the copper current collector.

Batteries & Supercaps

Research Article
doi.org/10.1002/batt.202300281

Chemistry Europe
European Chemical
Societies Publishing

an incomplete reoxidation – at least of tin (in line with the *operando* data). These results are generally in good agreement with the electrochemical data, pointing at an incomplete reoxidation and reformation of (amorphous) sodium oxide. The given findings also highlight the need for complementary *operando* and *ex situ* experiments – each with its limitations and benefits – to unveil such reaction mechanisms.

Further insights into the reaction mechanism were obtained by *ex situ* transmission electron microscopy (TEM) and energy-dispersive X-ray spectroscopy (EDX, coupled with STEM) on sodiated and desodiated $Sn_{0.9}Fe_{0.1}O_{2-\delta}$ electrodes (Figure 5a and b, respectively; for comparison the data for the pristine material are displayed in Figure 5c, d). The TEM micrograph of the sodiated sample (Figure 5a) reveals the formation of relatively large, few nanometer-sized grains, which appear to be tin with regard to the contrast and the accompanying EDX mapping (see also Figure S2 for TEM micrographs of the pristine material). Interestingly, the EDX mapping of sodium and iron indicates a rather homogeneous distribution, suggesting that (i) the metallic tin tends to cluster into fine nanograins more than iron, which is initially well distributed in the tin oxide crystal structure (Figure 5c, d)[27] – or simply forms even finer nanograins, and that (ii) the sodium oxide matrix, resulting from the initial sodiation, well surrounds the tin nanograins within the secondary particles (in addition to its presence in the SEI and conductive carbon). For the desodiated sample (Figure 5b), significantly larger primary particles were observed, indicating the (partial) reoxidation of the metallic phases and (partial) reformation of the sodium oxide matrix. Additionally, the iron and tin mapping are in rather good agreement, while a significant concentration of sodium appears to be present where there is little tin and iron. This finding – along with the reversible specific capacity and initial Coulombic efficiency suggests that the reformation of the sodium oxide matrix remains incomplete and that there is some sodium trapped in the conductive carbon and/or the SEI. The formation of the latter, though, appears to be somehow reversible, as there is a rather thick amorphous layer of a few nanometers observed for the sodiated material, surrounding the secondary particle (Figure 5a), which at least partially disappeared for the desodiated material (Figure 5b). Similar findings have been reported earlier, in fact, for comparable active materials studied as lithium-ion anodes.[25]

The important impact of the SEI on the electrochemical behavior was further evidenced by slightly modifying the electrolyte composition and adding 3 vol.% of fluoroethylene carbonate (FEC) to the electrolyte, as displayed in Figure 6. The comparison of the first cycle dis-/charge profiles (Figure 6a–c) reveals a decomposition of the FEC additive at above 1.0 V, resulting in a somewhat lower discharge capacity for all three materials, especially for SnO_2 (Figure 6a). Interestingly, though, also the charge capacity slightly decreases in the case of SnO_2 (Figure 6a) and $Sn_{0.9}Fe_{0.1}O_{2-\delta}$-C (Figure 6c), while it remains fairly constant for $Sn_{0.9}Fe_{0.1}O_{2-\delta}$ (Figure 6b), suggesting that the FEC-modified SEI (i) stabilizes the electrode|electrolyte interface by decreasing the electrolyte decomposition to some extent, while (ii) having an insulating effect that hinders the sodium
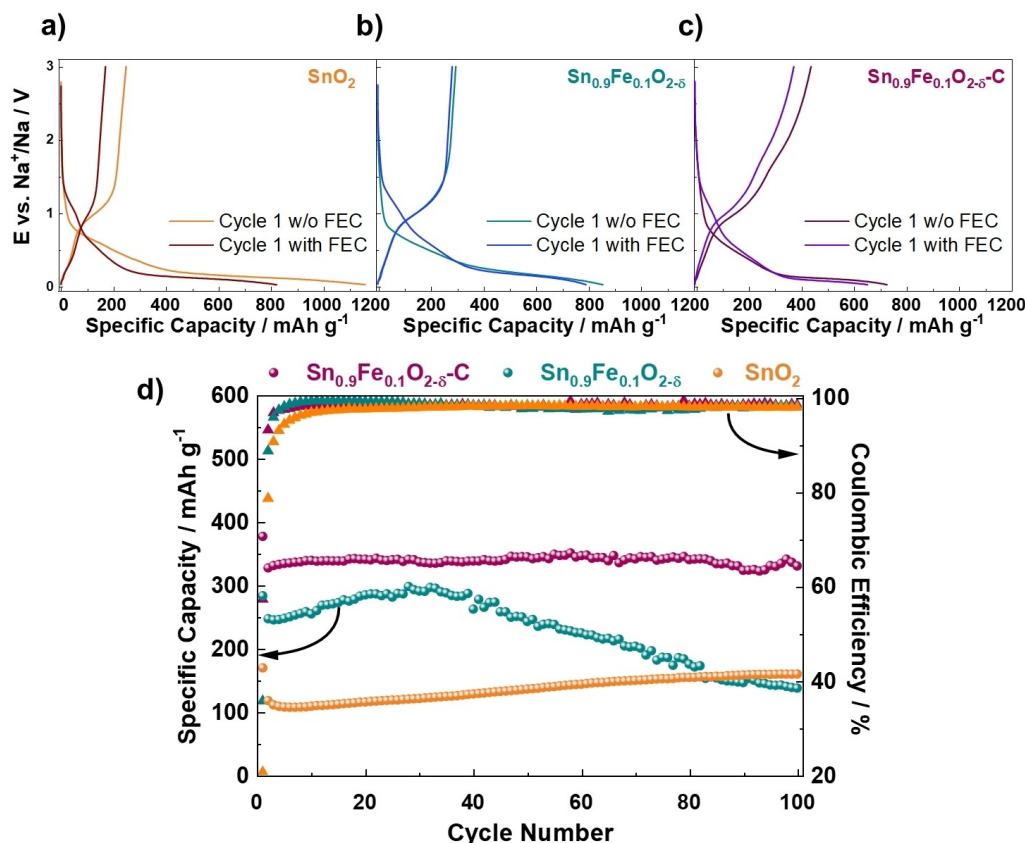
transport across the SEI. In the case of $Sn_{0.9}Fe_{0.1}O_{2-\delta}$, this effect might be less pronounced owing to the presence of metallic iron at the outermost surface of the particles, which is covered by carbon in the case of $Sn_{0.9}Fe_{0.1}O_{2-\delta}$-C. Nonetheless, this stabilizing effect (presumably benefitting from the more insulating nature of the SEI) results in a substantially enhanced cycling stability, especially for SnO_2 and $Sn_{0.9}Fe_{0.1}O_{2-\delta}$-C, yielding a very stable capacity of around 120 mAh g^{-1} (0.17 mAh cm^{-2}) and 340 mAh g^{-1} (0.44 mAh cm^{-2}), respectively, after 100 cycles, while the capacity continuously fades for $Sn_{0.9}Fe_{0.1}O_{2-\delta}$ after about 40 cycles (Figure 6d). Following the insights from the *ex situ/operando* XRD and *ex situ* TEM results as well as the insights gained from the investigations as lithium-ion anode material,[36] we may assume that the presence of iron and its reduction to the metallic state leads to an enhanced electronic conductivity, thus favoring the reversible formation of the sodium oxide species and a suppressed tin nanograin growth. Furthermore, the introduction of vacancies by aliovalent doping presumably facilitates the diffusion of the sodium cations within the metal oxide structure, which might add to the higher capacity by rendering the particle bulk more accessible.

Conclusions

The comparative electrochemical characterization of SnO_2, $Sn_{0.9}Fe_{0.1}O_{2-\delta}$, and $Sn_{0.9}Fe_{0.1}O_{2-\delta}$-C as potential sodium-ion anode candidates revealed a beneficial impact of the presence of iron and a carbon coating on the achievable reversible capacity and cycling stability. However, the sodiation and subsequent desodiation reaction remained incomplete, as indicated by the significant difference between the experimentally determined and theoretically expected capacity when assuming a complete alloying and conversion reaction. The *operando* and *ex situ* XRD analysis showed that this is (at least in part) due to the incomplete alloying (upon sodiation) and reconversion (upon desodiation) reaction of tin. The *ex situ* TEM/EDX further showed that a significant fraction of sodium remains irreversibly trapped in the material, the conductive carbon and the SEI. In fact, modifying the electrolyte composition by adding FEC led to a substantially enhanced cycling stability, though at the expense of reversible capacity – both presumably related to an increased insulating nature of the FEC-derived SEI. These results show that the reaction mechanism of $Sn_{0.9}Fe_{0.1}O_{2-\delta}$ with sodium is generally comparable to the reaction with lithium, while further studies are needed to unveil the factors that limit the de-/sodiation reaction in order to obtain further enhanced reversible capacities for such electrode materials. Additionally, further electrolyte optimization and/or the combination with suitable pre-sodiation strategies might enable further improvement of the achievable capacity, cycling stability, and (first cycle) Coulombic efficiency.
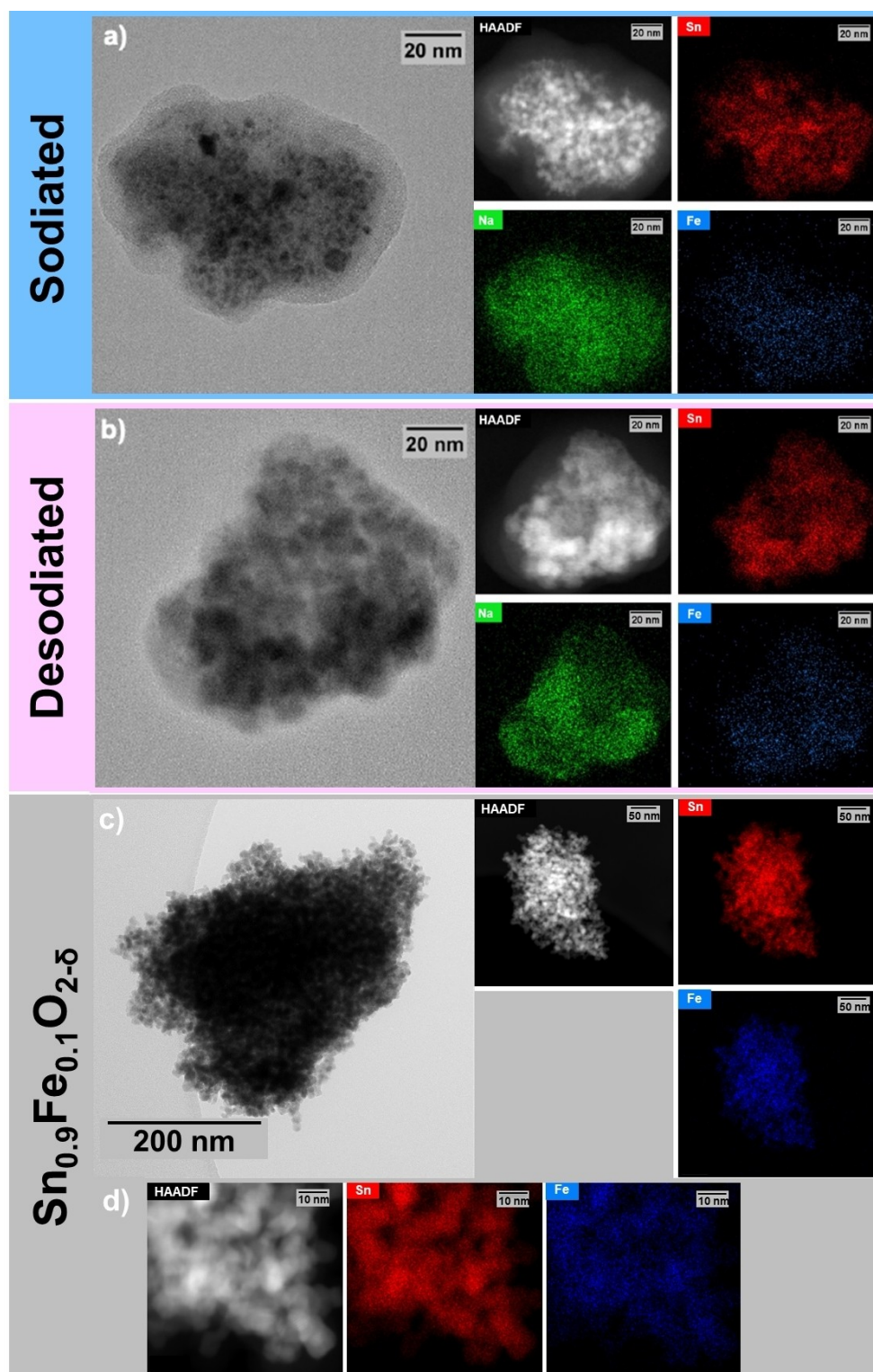
Figure 5. TEM and STEM/EDX micrographs for a) sodiated (0.01 V), b) desodiated $Sn_{0.9}Fe_{0.1}O_{2-\delta}$ (3.0 V) and c, d) pristine $Sn_{0.9}Fe_{0.1}O_{2-\delta}$ at two different magnifications, using the high-angle annular dark-field (HAADF) detector for STEM images and the corresponding EDX mapping of Sn (red), Na (green), and Fe (blue).

Batteries & Supercaps

Research Article
doi.org/10.1002/batt.202300281

**Chemistry
Europe**

European Chemical
Societies Publishing

Figure 6. a–c) Dis-/Charge profiles of the 1st galvanostatic cycle at 50 mA g^{-1} for a) SnO$_2$, b) Sn$_{0.9}$Fe$_{0.1}$O$_{2-\delta}$, and c) Sn$_{0.9}$Fe$_{0.1}$O$_{2-\delta}$-C vs. metallic sodium with and without FEC in the electrolyte. d) Plot of the cycle number vs. specific capacity and Coulombic efficiency for SnO$_2$, Sn$_{0.9}$Fe$_{0.1}$O$_{2-\delta}$ and Sn$_{0.9}$Fe$_{0.1}$O$_{2-\delta}$-C vs. sodium metal in presence of FEC in the electrolyte (1st cycle: 50 mA g^{-1}; following cycles: 100 mA g^{-1}; cut-off potentials: 0.01 and 3.00 V vs. Na$^+$/Na).

Experimental Section

Synthesis of the active material

The synthesis of the three active materials followed the same procedure reported earlier.[35,36] In brief, iron-doped tin (IV) oxide (Sn$_{0.9}$Fe$_{0.1}$O$_{2-\delta}$) was synthesized by dissolving iron (II) gluconate dihydrate (0.001 mol; Alfa Aesar) and sucrose (0.030 mol; Merck) in 100 mL ultrapure H$_2$O. Subsequently, 20 mL of acetic acid (Sigma Aldrich) and tin (II) acetate (0.009 mol; Alfa Aesar) were added gradually and stirred for 1.5 h. The resulting solution was heated to 50 °C for 30 min, before the water was evaporated at 180 °C. The remaining black solid was dried at 80 °C overnight. Subsequently, it was manually ground in a mortar and the resulting powder was calcined at 450 °C for 3 h under ambient atmosphere (heating rate: 3 °C min^{-1}). Pure tin (IV) oxide (SnO$_2$) was prepared accordingly, just without the addition of the iron precursor. Carbon-coated iron-doped tin (IV) oxide (Sn$_{0.9}$Fe$_{0.1}$O$_{2-\delta}$-C) was prepared under hydro-thermal conditions. First, glucose (0.007 mol; VWR) was dissolved in 80 mL ultrapure H$_2$O. Then, 800 mg Sn$_{0.9}$Fe$_{0.1}$O$_{2-\delta}$ powder was added to the solution, before it was thermally treated in a stainless steel autoclave (Berghof BR-100) at 180 °C under continuous stirring for 13 h. The precipitate obtained *via* centrifugation was washed with ultrapure H$_2$O and ethanol and dried at 80 °C overnight. After drying, the powder was thermally treated at 500 °C for 4 h under argon atmosphere (heating rate: 3 °C min^{-1}). The investigation *via* thermogravimetric analysis (TGA) revealed a carbon content of about 13 wt.%.[36]

Electrode preparation

For the electrode preparation, 375 mg of the active material and 100 mg of conductive carbon (Super C65; Imerys) were manually mixed and added to a 1.25 wt% solution of sodium carboxymethyl cellulose (CMC; Dow Wolff Cellulosiscs) in ultrapure H$_2$O. The weight ratio of the active material, conductive carbon, and binder was 75:20:5. The dispersion was first mixed by stirring for 5 min and then further homogenized using a planetary ball mill (Vario-Planetary Mill Pulverisette 4; Fritsch). The obtained slurry was cast on dendritic Cu foil (Cu ≥ 99.9%; Schlenk) with a wet film thickness of 140 μm. The electrode sheet was dried overnight at room temperature and disc electrodes with a diameter of 12 mm were cut. Subsequently, the disc electrodes were dried under vacuum (10^{-3} mbar) at 120 °C for 12 h. The average active material mass loading in all three cases was about 1.3–2.0 mg cm^{-2}.

Electrochemical characterization

The electrochemical characterization was conducted in three-electrode Swagelok® cells using manually rolled sodium (99.8%, Acros Organics) as counter and reference electrodes. All cells were assembled in a glove box (MBraun UNIlab; H$_2$O and O$_2$ content < 0.1 ppm) under argon atmosphere. Glass microfiber sheets (GF/D; Whatman) were used as separator and these were drenched with a 1 M solution of NaPF$_6$ (battery grade; FluoroChem) in a 1:1 volume mixture of ethylene carbonate and diethyl carbonate (both UBE) serving as the electrolyte. For some experiments, 3 vol.% of fluoroethylene carbonate (FEC; BASF) were added to the electrolyte.

Batteries & Supercaps

Research Article
doi.org/10.1002/batt.202300281

Chemistry Europe
European Chemical
Societies Publishing

Galvanostatic cycling was carried out by means of a Maccor Battery Tester 4300 at $20 \pm 1\,°C$. Cyclic voltammetry (CV) was performed at $20\,°C \pm 2\,°C$ using a VMP3 potentiostat from BioLogic. The sweep rate was $0.1\,\mathrm{mV\,s^{-1}}$ in the voltage range from 0.01 to 3.0 V vs. Na^+/Na.

Operando XRD

For the *operando* XRD measurements, a self-designed two-electrode cell was used.[48] The slurry, comprising the active material, conductive carbon, and the binder in a weight ratio of $75:20:5$, was mixed as described above. The resulting dispersion was cast directly on a beryllium disc (25 mm diameter, 0.25 mm thickness; Materion), which served simultaneously as the current collector and "window" for the X-ray beam. The coated Be disc was dried for 12 h at room temperature and 60 °C under vacuum for 4 h. Metallic sodium was used as the counter and reference electrode and two GF/D separators ($\varnothing = 19\,mm$) drenched with 400 μL of the electrolyte served as the separator. Upon de-/sodiation, the XRD data were recorded in a 2θ range of $14° \leq 2\theta \leq 60°$.

Ex situ transmission electron microscopy

Ex situ transmission electron microscopy (TEM) and energy-dispersive X-ray spectroscopy was conducted by disassembling the cycled $Sn_{0.9}Fe_{0.1}O_{2-\delta}$-C half-cells in an argon-filled glove box, rinsing the electrodes with 100 μL DMC, drying them, and scraping off the active material from the copper current collector. A dedicated sample holder was used for the sample transfer from the glove box to the TEM in order to avoid any contact with air or moisture. The TEM/EDX analysis was performed using a Talos 200X (Thermo Fisher Scientific) equipped with a dedicated SuperX EDX detector working at an accelerating voltage of 200 kV.

Acknowledgements

Conflict of Interests

The authors declare no conflict of interest.

Data Availability Statement

The data that support the findings of this study are available from the corresponding author upon reasonable request.

[1] I. Hasa, J. Barker, G. Elia, S. Passerini, in *Reference Module in Chemistry, Molecular Sciences and Chemical Engineering*, Elsevier, **2023**.

[2] N. Tapia-Ruiz, A. R. Armstrong, H. Alptekin, M. A. Amores, H. Au, J. Barker, R. Boston, W. R. Brant, J. M. Brittain, Y. Chen, M. Chhowalla, Y.-S. Choi, S. I. R. Costa, M. Crespo Ribadeneyra, S. A. Cussen, E. J. Cussen, W. I. F. David, A. V. Desai, S. A. M. Dickson, E. I. Eweka, J. D. Forero-Saboya, C. P. Grey, J. M. Griffin, P. Gross, X. Hua, J. T. S. Irvine, P. Johansson, M. O. Jones, M. Karlsmo, E. Kendrick, E. Kim, O. V. Kolosov, Z. Li, S. F. L. Mertens, R. Mogensen, L. Monconduit, R. E. Morris, A. J. Naylor, S. Nikman, C. A. O'Keefe, D. M. C. Ould, R. G. Palgrave, P. Poizot, A. Ponrouch, S. Renault, E. M. Reynolds, A. Rudola, R. Sayers, D. O. Scanlon, S. Sen, V. R. Seymour, B. Silván, M. T. Sougrati, L. Stievano, G. S. Stone, C. I. Thomas, M.-M. Titirici, J. Tong, T. J. Wood, D. S. Wright, R. Younesi, *J. Phys. E* **2021**, *3*, 031503.

[3] C. Vaalma, D. Buchholz, M. Weil, S. Passerini, *Nat. Rev. Mater.* **2018**, *3*, 1–11.

[4] W. Zuo, A. Innocenti, M. Zarrabeitia, D. Bresser, Y. Yang, S. Passerini, *Acc. Chem. Res.* **2023**, *56*, 284–296.

[5] J.-Y. Hwang, S.-T. Myung, Y.-K. Sun, *Chem. Soc. Rev.* **2017**, *46*, 3529–3614.

[6] V. Palomares, P. Serras, I. Villaluenga, K. B. Hueso, J. Carretero-González, T. Rojo, *Energy Environ. Sci.* **2012**, *5*, 5884–5901.

[7] M. D. Slater, D. Kim, E. Lee, C. S. Johnson, *Adv. Funct. Mater.* **2013**, *23*, 947–958.

[8] J. Asenbauer, T. Eisenmann, M. Kuenzel, A. Kazzazi, Z. Chen, D. Bresser, *Sustain. Energy Fuels* **2020**, *4*, 5387–5416.

[9] X. Dou, I. Hasa, D. Saurel, C. Vaalma, L. Wu, D. Buchholz, D. Bresser, S. Komaba, S. Passerini, *Mater. Today* **2019**, *23*, 87–104.

[10] D. A. Stevens, J. R. Dahn, *J. Electrochem. Soc.* **2001**, *148*, A803.

[11] Y. Lu, L. Yu, X. W. (David) Lou, *Chem* **2018**, *4*, 972–996.

[12] D. Bresser, E. Paillard, P. Niehoff, S. Krueger, F. Mueller, M. Winter, S. Passerini, *ChemPhysChem* **2014**, *15*, 2177–2185.

[13] P. Poizot, S. Laruelle, S. Grugeon, L. Dupont, J.-M. Tarascon, *Nature* **2000**, *407*, 496–499.

[14] A. N. Dey, *J. Electrochem. Soc.* **1971**, *118*, 1547.

[15] O. Riedel, A. Düttmann, S. Dühnen, J. Kolny-Olesiak, C. Gutsche, J. Parisi, M. Winter, M. Knipper, T. Placke, *ACS Appl. Nano Mater.* **2019**, *2*, 3577–3589.

[16] B. Wang, J. Ryu, S. Choi, X. Zhang, D. Pribat, X. Li, L. Zhi, S. Park, R. S. Ruoff, *ACS Nano* **2019**, *13*, 2307–2315.

[17] G. A. Elia, D. Bresser, J. Reiter, P. Oberhumer, Y.-K. Sun, B. Scrosati, S. Passerini, J. Hassoun, *ACS Appl. Mater. Interfaces* **2015**, *7*, 22638–22643.

[18] Y. Xu, Y. Zhu, Y. Liu, C. Wang, *Adv. Energy Mater.* **2013**, *3*, 128–133.

[19] C.-Y. Chou, M. Lee, G. S. Hwang, *J. Phys. Chem. C* **2015**, *119*, 14843–14850.

[20] M. Hu, Y. Jiang, W. Sun, H. Wang, C. Jin, M. Yan, *ACS Appl. Mater. Interfaces* **2014**, *6*, 19449–19455.

[21] J. Asenbauer, A. Varzi, S. Passerini, D. Bresser, *J. Power Sources* **2020**, *473*, 228583.

[22] P. Yadav, G. Parte, W. Malik, Y. M. Sabri, L. A. Jones, M. V. Shelke, *Sustain. Energy Fuels* **2022**, *6*, 3806–3817.

[23] Y. Ma, Y. Ma, G. Giuli, T. Diemant, R. J. Behm, D. Geiger, U. Kaiser, U. Ulissi, S. Passerini, D. Bresser, *Sustain. Energy Fuels* **2018**, *2*, 2601–2608.

[24] M. Lübke, D. Ning, C. F. Armer, D. Howard, D. J. L. Brett, Z. Liu, J. A. Darr, *Electrochim. Acta* **2017**, *242*, 400–407.

[25] T. Eisenmann, J. Asenbauer, S. J. Rezvani, T. Diemant, R. J. Behm, D. Geiger, U. Kaiser, S. Passerini, D. Bresser, *Small Methods* **2021**, *5*, 2001021.

[26] T. Eisenmann, A. Birrozzi, A. Mullaliu, G. Giuli, A. Trapananti, S. Passerini, D. Bresser, *J. Electrochem. Soc.* **2021**, *168*, 030503.

[27] A. Birrozzi, A. Mullaliu, T. Eisenmann, J. Asenbauer, T. Diemant, D. Geiger, U. Kaiser, D. Oliveira de Souza, T. E. Ashton, A. R. Groves, J. A. Darr, S. Passerini, D. Bresser, *Inorganics* **2022**, *10*, 46.

[28] A. Birrozzi, J. Asenbauer, T. E. Ashton, A. R. Groves, D. Geiger, U. Kaiser, J. A. Darr, D. Bresser, *Batteries & Supercaps* **2020**, *3*, 284–292.

[29] V. L. Chevrier, G. Ceder, *J. Electrochem. Soc.* **2011**, *158*, A1011.

[30] W. T. Jing, C. C. Yang, Q. Jiang, *J. Mater. Chem. A* **2020**, *8*, 2913–2933.

[31] L. Baggetto, P. Ganesh, C.-N. Sun, R. A. Meisner, T. A. Zawodzinski, G. M. Veith, *J. Mater. Chem. A* **2013**, *1*, 7985–7994.

[32] J. Qian, Y. Chen, L. Wu, Y. Cao, X. Ai, H. Yang, *Chem. Commun.* **2012**, *48*, 7070–7072.

Batteries & Supercaps

Research Article
doi.org/10.1002/batt.202300281

Chemistry Europe
European Chemical
Societies Publishing

[33] Y. Kim, Y. Park, A. Choi, N.-S. Choi, J. Kim, J. Lee, J. H. Ryu, S. M. Oh, K. T. Lee, *Adv. Mater.* **2013**, *25*, 3045–3049.

[34] J. Qian, X. Wu, Y. Cao, X. Ai, H. Yang, *Angew. Chem.* **2013**, *125*, 4731–4734.

[35] F. Mueller, D. Bresser, V. S. K. Chakravadhanula, S. Passerini, *J. Power Sources* **2015**, *299*, 398–402.

[36] J. Asenbauer, A.-L. Wirsching, M. Lang, S. Indris, T. Eisenmann, A. Mullaliu, A. Birrozzi, A. Hoefling, D. Geiger, U. Kaiser, R. Schuster, D. Bresser, *Adv. Sustainable Syst.* **2022**, *6*, 2200102.

[37] J. Asenbauer, A. Hoefling, S. Indris, J. Tübke, S. Passerini, D. Bresser, *ACS Appl. Mater. Interfaces* **2020**, *12*, 8206–8218.

[38] D. Su, H.-J. Ahn, G. Wang, *Chem. Commun.* **2013**, *49*, 3131–3133.

[39] J. Ding, Z. Li, H. Wang, K. Cui, A. Kohandehghan, X. Tan, D. Karpuzov, D. Mitlin, *J. Mater. Chem. A* **2015**, *3*, 7100–7111.

[40] Y. Liu, F. Wang, L.-Z. Fan, *Nano Res.* **2018**, *11*, 4026–4037.

[41] A. Trapananti, T. Eisenmann, G. Giuli, F. Mueller, A. Moretti, S. Passerini, D. Bresser, *Mater. Today Chem.* **2021**, *20*, 100478.

[42] L. Xiao, Y. Cao, J. Xiao, W. Wang, L. Kovarik, Z. Nie, J. Liu, *Chem. Commun.* **2012**, *48*, 3321–3323.

[43] D. Dixon, M. Ávila, H. Ehrenberg, A. Bhaskar, *ACS Omega* **2019**, *4*, 9731–9738.

[44] L. D. Ellis, T. D. Hatchard, M. N. Obrovac, *J. Electrochem. Soc.* **2012**, *159*, A1801.

[45] D. Bresser, F. Mueller, D. Buchholz, E. Paillard, S. Passerini, *Electrochim. Acta* **2014**, *128*, 163–171.

[46] H. Zhang, I. Hasa, S. Passerini, *Adv. Energy Mater.* **2018**, *8*, 1702582.

[47] I. Hasa, S. Mariyappan, D. Saurel, P. Adelhelm, A. Y. Koposov, C. Masquelier, L. Croguennec, M. Casas-Cabanas, *J. Power Sources* **2021**, *482*, 228872.

[48] D. Bresser, E. Paillard, R. Kloepsch, S. Krueger, M. Fiedler, R. Schmitz, D. Baither, M. Winter, S. Passerini, *Adv. Energy Mater.* **2013**, *3*, 513–523.
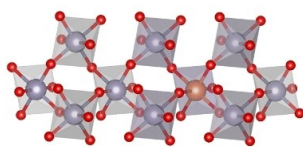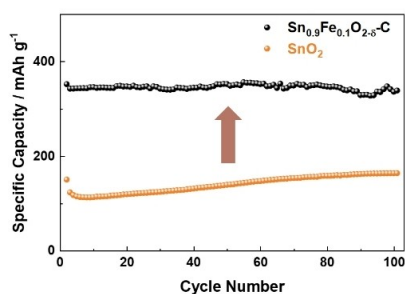
RESEARCH ARTICLE

A. Lenzer, Dr. A. Birrozzi, A.-L. Wirsching, Dr. Y. Li, Dr. D. Geiger, Prof. Dr. U. Kaiser, Dr. J. Asenbauer*, Dr. D. Bresser*

1 – 10

Evaluation of Sn$_{0.9}$Fe$_{0.1}$O$_{2-\delta}$ as Potential Anode Material for Sodium-Ion Batteries

New insights: Doping SnO$_2$ with iron combined with a carbon coating and fluoroethylene carbonate as electrolyte additive results in a triplication of the reversible capacity. The compre- hensive electrochemical characteriza- tion coupled with *ex situ/operando* XRD and TEM yields valuable insights into the impact of the iron dopant and the remaining challenges.